



Structural, Impedance, and Leakage Current Characteristics of Stannum Modified $\text{Bi}_{0.5}\text{Na}_{0.5}\text{TiO}_3$ Ceramic

Neeha Pradhani¹ · P. K. Mahapatra¹ · R. N. P. Choudhary¹

Received: 19 June 2020 / Accepted: 27 July 2020 / Published online: 7 August 2020
© Springer Science+Business Media, LLC, part of Springer Nature 2020

Abstract

A perovskite ceramic oxide, stannum (Sn) modified bismuth sodium titanate (BNT) (i.e., $\text{Bi}_{0.5}\text{Na}_{0.5}\text{Ti}_{0.80}\text{Sn}_{0.20}\text{O}_3$) was synthesized by using a mixed oxide powder reaction route. Analysis of the X-Ray diffraction spectrum supports the polycrystalline nature of the compound with tetragonal symmetry. A phase change from the ferroelectric to paraelectric transition is observed at around 315 °C. The temperature and frequency dependence of dielectric properties and AC conductivity data of the material are analyzed. The Nyquist plots explain the effect of the grain and grain boundary contribution on the polarization process of the material. The analysis of complex modulus spectroscopy exhibits the non-Debye relaxation in the compound. The doping of stannum at the titanium-site of BNT enhances the dielectric characteristics of the material.

Keywords X-ray diffraction · Dielectric spectroscopy · Nyquist plot · Leakage current

1 Introduction

ABO_3 type perovskite oxides, especially PbTiO_3 , have found potential device applications, like switches, capacitors, light modulators, sensors, transducers, nonvolatile memory, thermistors, optoelectronic devices, and infrared imaging [1]. Search for new ferroelectric compounds with this structure arose to minimize the industrial use of toxic Pb. $\text{Bi}_{0.5}\text{Na}_{0.5}\text{TiO}_3$ (BNT) is found to be a good replacement for PbTiO_3 having a similar electronic configuration of Bi^{3+} ion $4f^{14}5d^{10}6s^2$ with a lone pair of 6S electrons as that in Pb^{2+} ion [2] and possess a high dielectric constant in a wide range of the temperature and strong ferroelectric properties with many industrial applications. BNT is also reported to exhibit two phase transitions; one at 200 °C corresponds to ferroelectric to relaxor ferroelectric and other at 320 °C corresponds to the relaxor ferroelectric to paraelectric phase transitions [3]. BNT is of ABO_3 type perovskite where complex occupations at the A/B- sites are possible, albeit with the combined electronic charge of the A-site ions is +1 or +2 and that of B is +5 or +4 respectively [4]. BNT is found to

be a superior ferroelectric at room temperature with a high value of the remnant polarization (P_r) of $38\mu\text{C}/\text{cm}^2$ [5]. Although it has several good properties, there are some drawbacks, like a high coercive field with difficulty in poling and high leakage current with difficulty in the measurement of intrinsic properties. Some drawbacks of the material can be overcome by a variety of methods, including doping/substitution at the A and/or B sites. While selecting the different ions for substitution in these perovskite structure compounds, emphasis should be laid on the charge neutrality and the tolerance factor. The tolerance factor which provides the basic information of geometric packing in perovskite (ABO_3) is expressed as $t' = \frac{r_A+r_O}{\sqrt{2}(r_B+r_O)}$, where r_A , r_B , and r_O are the average ionic radius of A-site and B- site atom and oxygen (O^{2-}) respectively [6]. Depending on the tolerance factor, the materials of the perovskite family crystallize in distinct structures, such as (i) $0.9 < t' < 0.97$ for cubic, (ii) $0.97 < t' < 1.02$ for tetragonal, and (iii) $0.8 < t' < 0.9$ for orthorhombic/monoclinic structure [7], which strongly influence the polarization property. Stannum as a compound in oxide form is one of the important metal oxides with a wide optical energy band gap, $E_g = 3.6$ eV at room temperature [8] and high-dielectric constant (18). The unique optical, electrochemical, electronic and catalytic properties make stannic oxide an important functional material in applications like solar cells, optoelectronic devices, gas sensors, laser diodes and transparent conducting electrode [9, 10].

✉ Neeha Pradhani
neeha.pradhani@gmail.com

¹ Department of Physics, Multiferroic Advanced Materials Laboratory, Siksha 'O' Anusandhan (Deemed To Be University), Bhubaneswar 751030, India

The electrical properties of stannic oxide are making it more useful in technology. While the stoichiometric form of stannic oxide exhibits insulating nature, that in non-stoichiometric form promotes oxygen vacancies and acts as a n-type semiconductor [11]. Further, the ionic radius of Sn^{4+} (0.69 Å) is relatively close to Ti^{4+} (0.605 Å), which makes it suitable for the formation of single phase compound. Keeping in the view of the wide applications of stannum in oxide form and high value of the dielectric constant, we have prepared stannum modified BNT i.e. $\text{Bi}_{0.5}\text{Na}_{0.5}\text{Ti}_{0.80}\text{Sn}_{0.20}\text{O}_3$ (BNTS) by cost-effective solid-state reaction mechanism.

2 Experimental and Characterization Techniques

The stannum modified BNT i.e. $\text{Bi}_{0.5}\text{Na}_{0.5}\text{Ti}_{0.80}\text{Sn}_{0.20}\text{O}_3$ (BNTS) was synthesized by a mixed oxide reaction technique. The stoichiometric ratio of high purity Bi_2O_3 (99.0%, Himedia), Na_2CO_3 (99.5%, CDH), TiO_2 (99.5%, Loba Chemie) and SnO_2 (99.9%, Loba Chemie) were taken in an agate mortar and mixed thoroughly in the dry state as well as in the wet mode using methanol for 3 h. The homogeneous fine raw powder was taken in a crucible and calcined at 900 °C for 4 h using a high-temperature furnace. Powder X-Ray diffractometer (Rigaku Ultima IV) was used for confirming the structural characteristics of the calcined powder. The pellet was prepared by KBR hydraulic press taking polyvinyl alcohol as a binder in the calcined powder and the pellets were sintered at 1050 °C for 4 h.

The silver coat was painted on both sides of sintered pellets for the electrode and heated at 100 °C for 45 min to get the moisture-free surface. The dielectric and electrical properties were measured through a phase-sensitive multimeter (N4L, Impedance Analysis Interface, and Model PSM-1735). The leakage current was measured by a Keithley electrometer (6517B). Marine India PE hysteresis loop tracer was used to investigate the ferroelectric properties of the compound. The schematic synthesis process and characterization has been presented in Fig. 1.

3 Results and Discussion

3.1 X-Ray Diffraction Study

The X-Ray Diffraction (XRD) spectrum of the BNTS ceramic compound is shown in Fig. 2. As the determined tolerance factor (t') of the material is found in between 0.97 and 1.02, the compound is expected to crystallize in the tetragonal symmetry. The indexing of the diffraction peaks has been done using standard 'Powd Mult' software. The XRD analysis supports the crystallization of the sample in

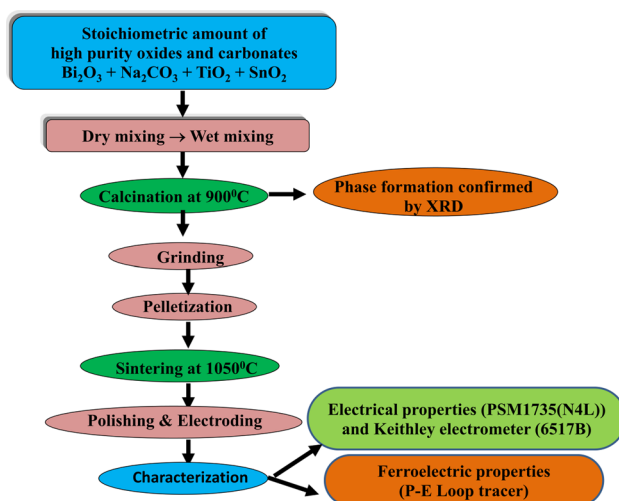


Fig. 1 Schematic diagram of synthesis and characterization of $\text{Bi}_{0.5}\text{Na}_{0.5}\text{Ti}_{0.80}\text{Sn}_{0.20}\text{O}_3$ by the mixed oxide reaction technique

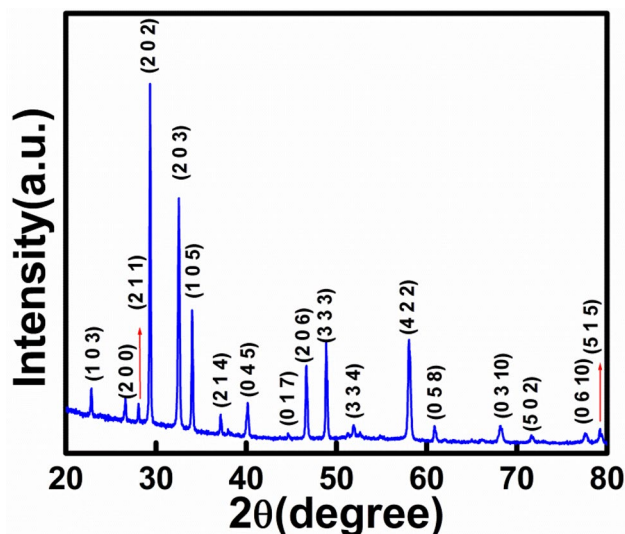


Fig. 2 XRD pattern of $\text{Bi}_{0.5}\text{Na}_{0.5}\text{Ti}_{0.80}\text{Sn}_{0.20}\text{O}_3$ compound

a tetragonal structure. The selection of the cell parameters of the compound is based on the good match of the interplanar spacing between the experimental and calculated value for each reflection with a negligibly small standard deviation. The selection of the cell parameters of the compound was done on the basis of a good fit, and the least-squares refinement procedure. The lattice constants, the c/a ratio, and volume of the sample are: $a = b = 6.6941$ Å, $c = 14.3407$ Å, $c/a = 2.1423$, and volume = 642.62 (Å)³ respectively. The crystallite (p) size of the specimen is estimated by using the diffraction profile data (i.e., diffraction angle, peak width, and optimization constant) and the wavelength of radiation in the Scherrer equation, $p = \frac{0.94\lambda}{\beta \cos\theta}$

[12–14]. The crystallite size amounts to 41 nm for the compound.

3.2 Effect of Temperature on Dielectric Property

The effect of temperature on the relative dielectric constant (ϵ'_r) and tangent loss ($\tan\delta$) of the BNTS compound at some chosen frequencies is shown in Fig. 3a and b. In Fig. 3a, we have observed a peak representing the ferroelectric to paraelectric phase transition at around 315 °C in the ϵ'_r vs. temperature graph. As mentioned in the introduction, the BNT exhibit two phase transitions; one at 200 °C corresponding to the ferroelectric to relaxor ferroelectric and other at 320 °C corresponding to the relaxor ferroelectric to paraelectric phase transition [15]. In our compound, we have not observed the ferroelectric to relaxor ferroelectric transition. At 1 kHz frequency, the value of ϵ'_r of the sample increases from 656 at room temperature to 3213 at the phase transition

temperature of 315 °C. For pure BNT, the reported value of ϵ'_r lies in the range of 516–1586 under similar temperature and frequency condition [16]. The substitution of Sn^{4+} at Ti^{4+} sites improves the dielectric constant. The increase is more in the higher temperature part as the thermal energy provides the necessary activation energy for the charge carriers to orient along the field. The value of the ϵ'_r increases as a result of the alignment of the polar molecules in the direction of the applied electric field.

From Fig. 3b, it is noticed that the loss increases with an increase in the temperature. The increase is more noticeable at lower frequencies in the higher temperature region due to increased conductivity. The compound with a dielectric constant of 510 and a dielectric loss of 0.03 at 25 °C and 1 MHz have good potentiality for device application.

3.3 Effect of Frequency on Dielectric Constant and Tangent Loss

Figure 4a shows the frequency variation of ϵ'_r of the material at chosen temperatures (100–250 °C). The variation of ϵ'_r in the experimental range of the frequency is due to the space charge and dipolar polarization. The space charge polarization and some mode of the dipolar polarization cease, as we move from low to high-frequency, and as a result, the dielectric constant reduces on increasing frequency in the entire range of the temperature [17]. Figure 4b depicts the frequency dependence loss tangent at variant temperatures. The tangent loss value is very less in the entire temperature and frequency range, which makes this compound suitable for device applications.

3.4 Impedance Spectroscopy

The impedance spectroscopy has been studied for the electrical characterization of the compound in a wide range of the frequency. The real (Z') and imaginary (Z'') component of the complex impedance analysis explain the bulk, grain boundary, and the electrode interface parts along with the relaxation process of the compound. In Fig. 5a, the value of Z' declines with an increment in frequency. For the selected range of temperature, the Z' values are almost similar above 100 kHz and coincide at a higher frequency apparently due to the release of the space charges. In a certain frequency range, the value of Z' increases with increasing temperature from 100 °C up to around 200 °C and then decreases, implying the positive temperature coefficient of resistance (PTCR) nature in the specimen up to 200 °C [18]. The PTCR nature signifies the reduction in the hopping process of the ions with increasing temperature. Above 200 °C, the activation of charge carriers dominate and the resistance decreases.

Figure 5b represents the variation of the imaginary component (Z'') of impedance with the frequency. Z'' decreases

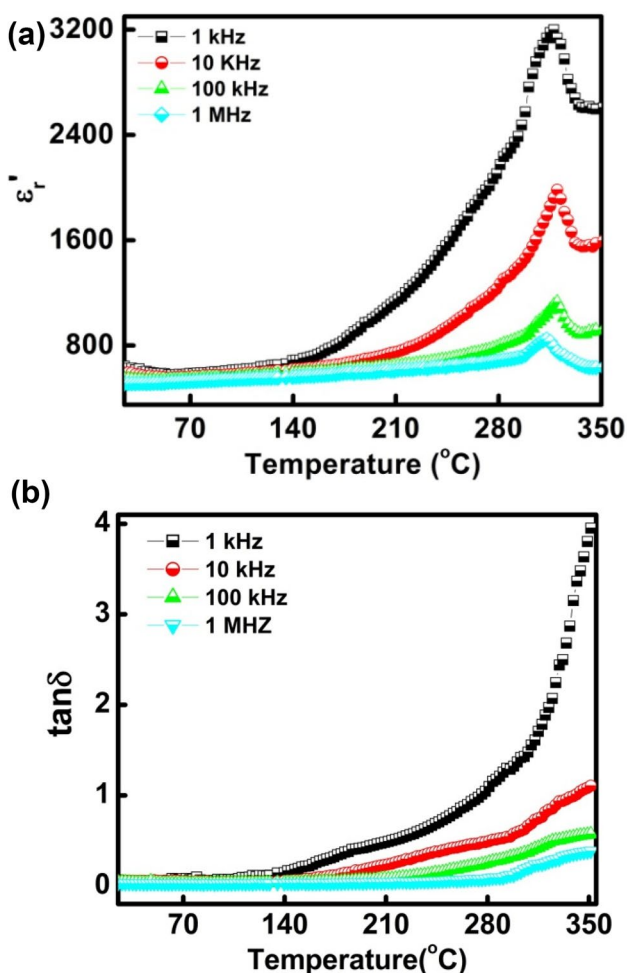


Fig. 3 **a** Effect of temperature on the ϵ'_r at some chosen frequencies of the compound. **b** Effect of temperature on $\tan\delta$ at selected frequencies of $\text{Bi}_{0.5}\text{Na}_{0.5}\text{Ti}_{0.80}\text{Sn}_{0.20}\text{O}_3$

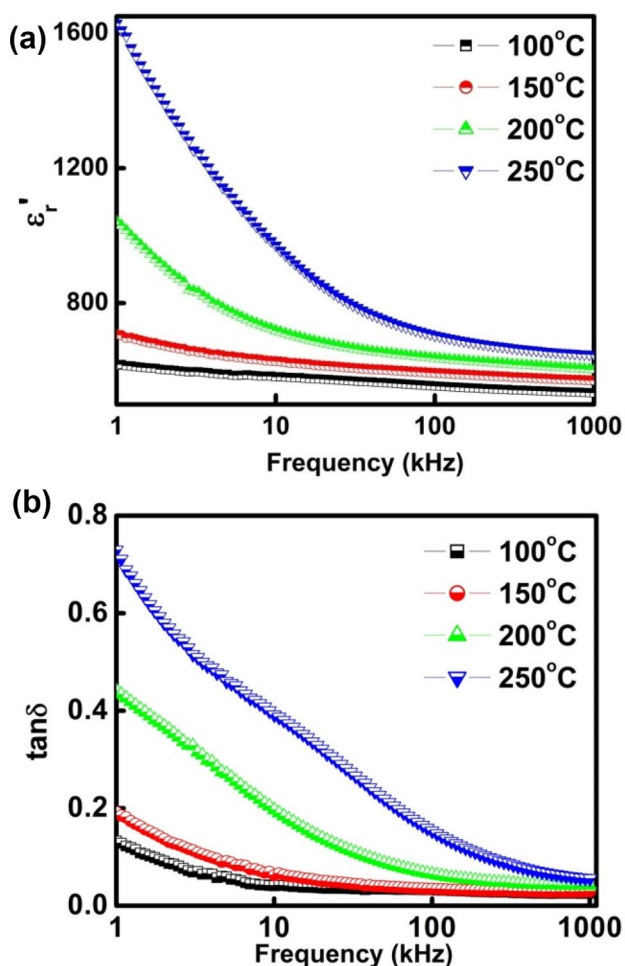


Fig. 4 a Effect of frequency on ϵ'_r at selected temperatures of the compound. b Effect of frequency on $\tan\delta$ at some chosen temperatures of $\text{Bi}_{0.5}\text{Na}_{0.5}\text{Ti}_{0.80}\text{Sn}_{0.20}\text{O}_3$

with a rise in frequency and beyond 100 kHz show the insensitivity to the frequency change for the entire temperature range of the experiment.

Figure 5c shows a Nyquist plot (Z'' vs. Z') of BNTS compound ceramics in the temperature range of 100–250 °C. The plot of impedance (Z) in the complex plane used to resolve the contributions from the bulk, grain boundary, and the electrode interface contribution to the polarization process. Each of these effects are represented by a semicircular arc in the complex impedance graph and designed by an equivalent circuit element of resistance (R) and capacitance (C). For ideal material, the perfect semicircular curve with center on the Z' -axis shows the ideal Debye relaxation mechanism. The inhomogeneity in the size of the grain and the electromagnetic diffusion in the ceramic compound affects the nature of the semicircular curve and it gets inclined to the real axis implying a distribution in the relaxation time [19–21]. The plot is fitted to the equivalent circuit of (RQC)

for 100 °C and 150 °C and (RQC) (RC) for 200 °C and 250 °C using the ZSIMPWIN software. The Q is defined as the constant phase element and signifies a deflection from the ideal Debye nature. The net electrical characteristic of the specimen is obtained by the series connection of both the grain and grain boundary contributions. The obtained parameters, i.e. grain resistance (R_g), capacitance (C_g), grain boundary resistance (R_{gb}), and capacitance (C_{gb}) from the Zsimpwin software are listed in Table 1.

The semicircular curve for the temperature of 150 °C is plotted by selecting three combinations of Z'' and Z' from the observed value and fitted with a circle equation [22]. Figure 5d represents the Nyquist plot at 150 °C with the depression angle (θ) of 2.29°.

3.5 AC Conductivity

Figure 6a depicts the graph of AC conductivity (σ_{ac}) with $1000/T$ in a wide range of the frequency. The AC conductivity is defined by the relation, $\sigma_{ac} = \epsilon_0 \epsilon'_r \omega \tan\delta$, and computed from the impedance data, where, the parameters having their usual definition. The high value of AC conductivity at the higher temperature is due to activation of more number of charge carriers. The movement of charge carriers increases through the hopping mechanism between the two sites. The activation energy is calculated by using the equation, $\sigma_{ac} = Ae^{-\frac{E_a}{k_B T}}$ [23]. The calculated activation energy at the higher temperature decreases with an increase in frequency. The increase in hopping probability with an increase in frequency between the localized sites reduces the activation energy. The low value of activation energy in the perovskite compounds correlates to the higher amounts of oxygen vacancies.

Figure 6b represents the frequency dependence AC conductivity for the BNTS compound within a range of the temperature 100–250 °C. The variation of frequency with AC conductivity is defined as, $\sigma_{ac}(\omega) = A\omega^s$ where A and s (≤ 1) are the polarizability factor and temperature-dependent frequency exponent respectively [24]. There are two slopes in the plot corresponding to the low-frequency and the high-frequency region respectively and the linear fitting on the log–log scale determines the value of s . The variation of s with temperature in different frequency regions indicates the conduction mechanisms active in the compound.

The variation of s in the low and high frequency regions behaves opposite to each other and it is shown in Fig. 6c and d. In the low-frequency region, the value of s increases with increasing temperature signifying the non-overlapping small polaron tunneling (NSPT) based conduction mechanism. In the high-frequency region, s decreases with increase in temperature suggesting the correlated barrier hopping (CBH) conduction mechanism in the material.

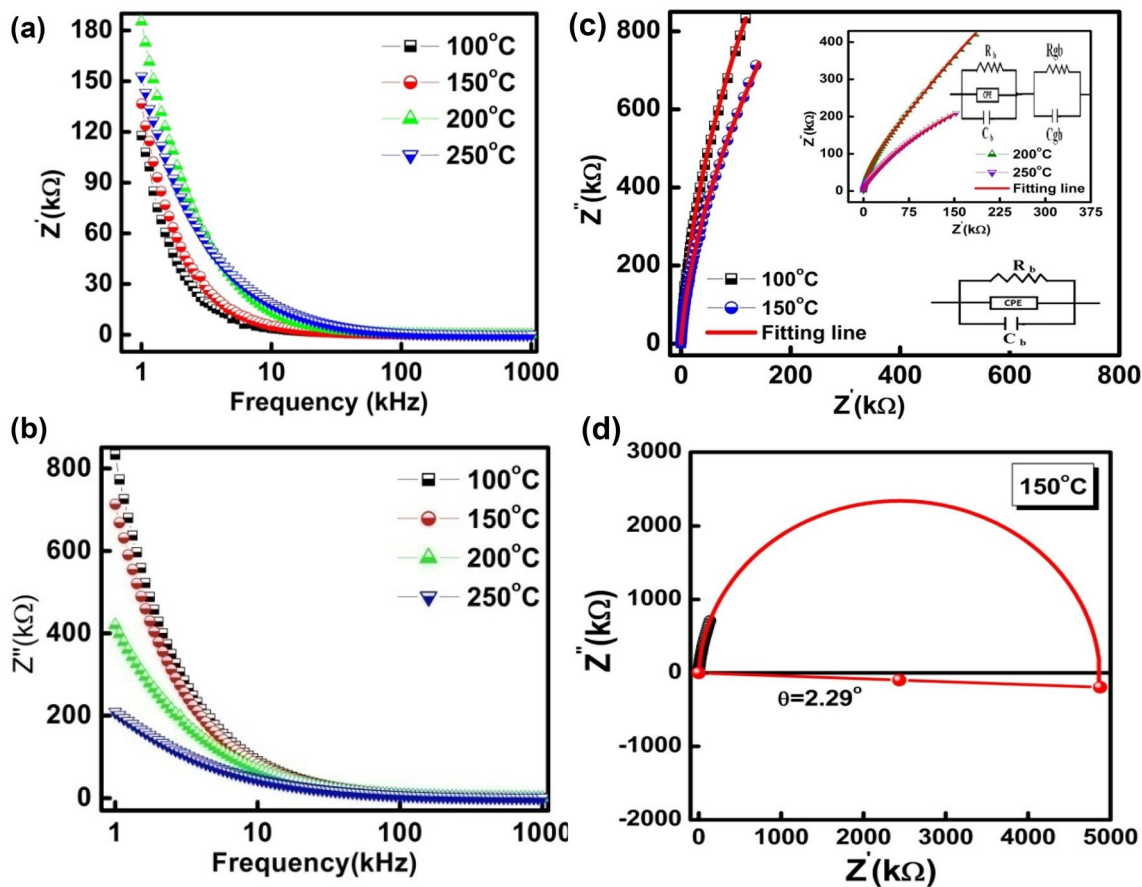


Fig. 5 **a** Frequency variation of Z' of $\text{Bi}_{0.5}\text{Na}_{0.5}\text{Ti}_{0.80}\text{Sn}_{0.20}\text{O}_3$ compound. **b** Variation of Z'' with frequency of $\text{Bi}_{0.5}\text{Na}_{0.5}\text{Ti}_{0.80}\text{Sn}_{0.20}\text{O}_3$ compound. **c** Z'' vs. Z' plot with the fitting of an equivalent circuit of

the compound. **d** Nyquist plot with semicircular curve fitting for the temperature of 150 °C of $\text{Bi}_{0.5}\text{Na}_{0.5}\text{Ti}_{0.80}\text{Sn}_{0.20}\text{O}_3$ compound

Table 1 R_g , C_g , R_{gb} , and C_{gb} at various temperatures of the compound

Temperature (°C)	R_g (kΩ)	C_g (pF)	R_{gb} (kΩ)	C_{gb} (pF)
100	8569	142	–	–
150	5381	166	–	–
200	161.1	298.4	4921	415.5
250	133.8	210.2	1891	656

The frequency exponent s for the NSPT model is given by [25]

$$s = 1 - \frac{4}{\ln\left(\frac{1}{\omega\tau_0}\right) - W_H/K_B T}$$

In the CBH model the temperature-dependent frequency exponent(s) is given by the equation [26]:

$$s = 1 - \frac{6K_B T}{W_M + K_B T \ln(\omega\tau_0)}$$

3.6 Modulus Analysis

The spectroscopic data of both modulus and impedance have importance in analyzing different electrical components and characteristics of the compound. The electric modulus can explain the electric features like the bulk and grain boundary effect, conduction properties, and relaxation time [27].

The complex electric modulus (M) is explained by using the impedance data relation, $M = M' + jM''$. The real part of modulus is defined by the relation, $M' = (-1)\omega C_0 Z''$ and the imaginary part as, $M'' = \omega C_0 Z'$. C_0 defines the geometrical capacitance calculated using $\epsilon_0 A/d$. In Fig. 7a, the M' value in the low-frequency part tends towards zero value. This feature indicates the hindrances in the movement of the charge carriers at low frequency. The M' value rises with an increasing frequency as the ions vibrate within the limits of their potential energy wells with the change of

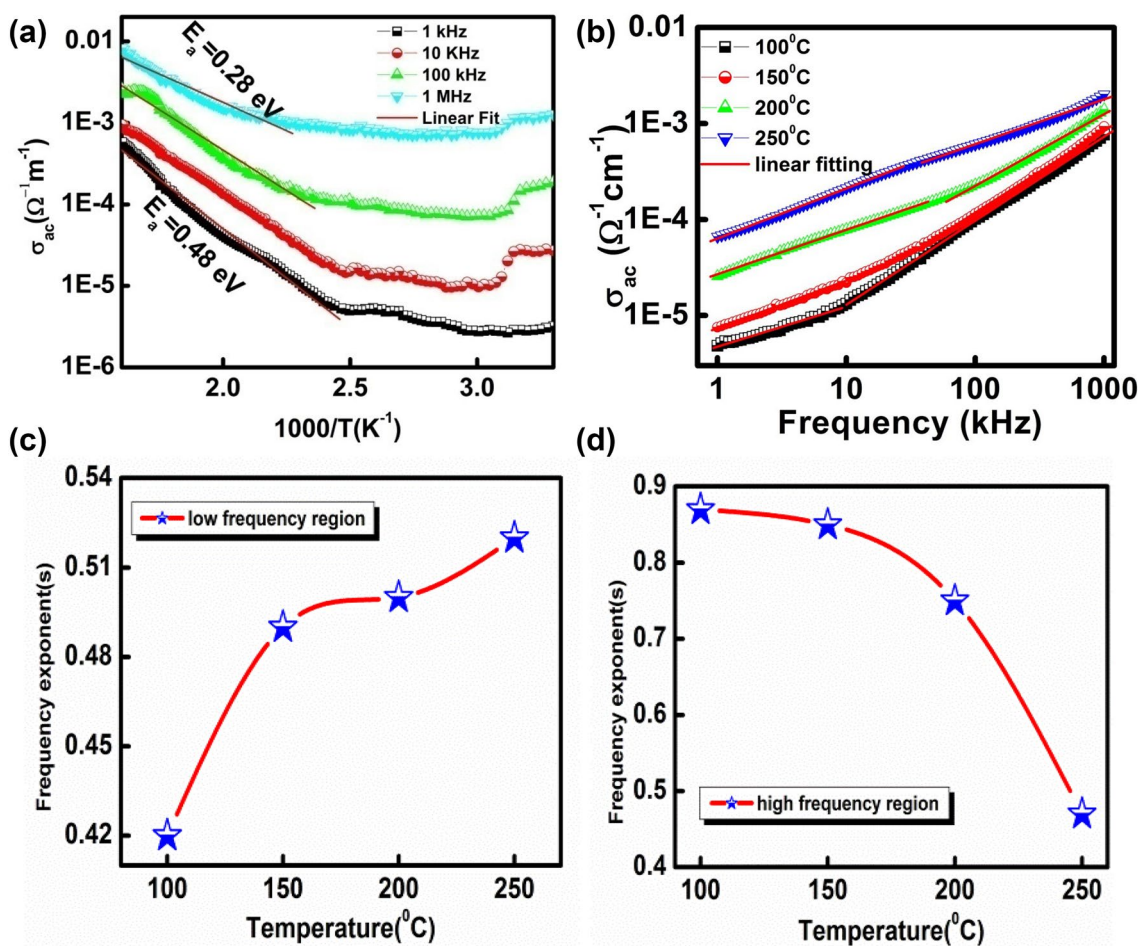


Fig. 6 **a** Effect of temperature on σ_{ac} of $\text{Bi}_{0.5}\text{Na}_{0.5}\text{Ti}_{0.80}\text{Sn}_{0.20}\text{O}_3$ compound. **b** Variation of σ_{ac} with frequency of the compound. Variation of frequency exponent (s) with the temperature, **(c)** in low-frequency, and **(d)** in high-frequency region of $\text{Bi}_{0.5}\text{Na}_{0.5}\text{Ti}_{0.80}\text{Sn}_{0.20}\text{O}_3$ compound

the electric field. The saturated part in the high-frequency part indicates the insensitiveness to the fast variation in the electric field.

Figure 7b represents the frequency variance of M'' of the BNTS compound at some selected temperatures. Peaks are observed in the temperature of 200 °C and 250 °C, which moves to the high-frequency with increasing temperature implying some kind of relaxor nature and the relaxation mechanism is due to the thermally activated ions. The relaxation peaks owe their existence to the limits of the ions in their potential energy well. The features of the low temperature graphs indicate the presence of peaks in the lower frequency region, which is beyond our experimental frequency range. The shifting of peak position in M'' suggests some sort of transition from the long to the short-range movement of the charge carriers with increasing frequency [28]. The presence of asymmetry peak signifies the relaxation time distribution leading to the non-Debye relaxation process in the materials. This type of mechanism occurs in ionic conductors [29].

3.7 Leakage Current

The room temperature J–E characteristic is studied from the I–V data for the BNTS compound is shown in Fig. 8a. The measured current density (J) at the electric field (E) of 30 V/cm is 3.4×10^{-10} A/cm². The charge transport mechanism in the perovskite oxides was explained with a fitting of the logarithmic J–E curve with several models like Schottky emission, Poole–Frenkel (PF) emission, Fowler–Nordheim (FN) tunnelling, and Space-Charge-Limited-Current conduction (SCLC) [30]. The linear fitting of $\log J$ vs. $\log E$ graph for the compound in Fig. 8b provides the value of the slope ~ 1 which signifies that the conduction mechanism is dominated by Ohmic characteristics.

3.8 Ferroelectric Property

The ferroelectric property of the compound is measured at room temperature and shown in Fig. 9 as polarization versus electric field loop. The hysteresis loop exhibit a remnant

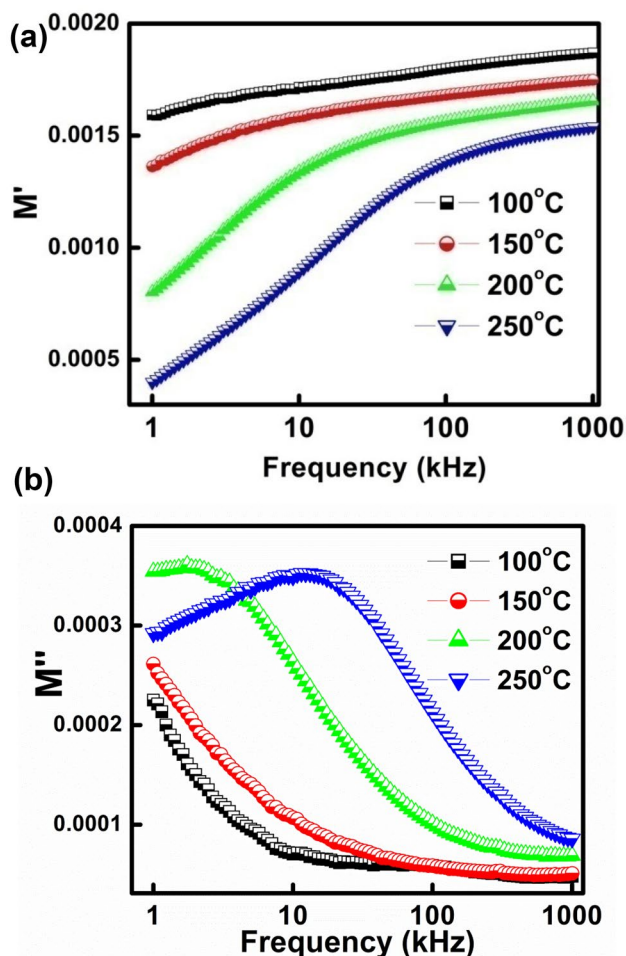


Fig. 7 **a** Frequency variation of M' of at some selected temperatures of the compound. **b** Variation of M'' with frequency of $\text{Bi}_{0.5}\text{Na}_{0.5}\text{Ti}_{0.80}\text{Sn}_{0.20}\text{O}_3$ compound

polarization (P_r) of $4.46 \mu\text{C}/\text{cm}^2$ and a coercive field (E_c) of $6.44 \text{ kV}/\text{cm}$. The well-defined and saturated observed loop suggest the ferroelectric nature of the compound.

4 Conclusion

$\text{Bi}_{0.5}\text{Na}_{0.5}\text{Ti}_{0.80}\text{Sn}_{0.20}\text{O}_3$ compound was fabricated by a cost-effective mixed oxide reaction route at the calcination and sintering temperature of 900°C and 1050°C respectively. The XRD analysis confirms that the compound crystallizes with the tetragonal structure. The frequency and temperature-dependent dielectric properties were studied in the material. The ferroelectric to paraelectric phase transition is noticed at 315°C in the temperature-dependent dielectric constant graph. The high dielectric constant and small tangent loss of the material at room temperature is suitable for device applications. The tilted semicircle and the presence

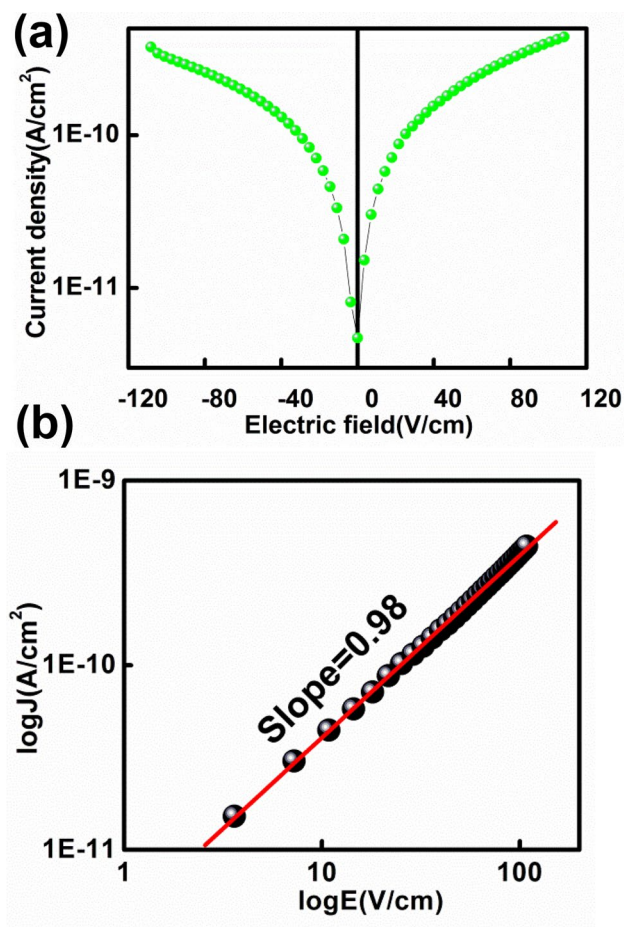


Fig. 8 **a** Leakage current density as a function of the electric field, and **b** $\log J$ vs. $\log E$ plot of $\text{Bi}_{0.5}\text{Na}_{0.5}\text{Ti}_{0.80}\text{Sn}_{0.20}\text{O}_3$ compound

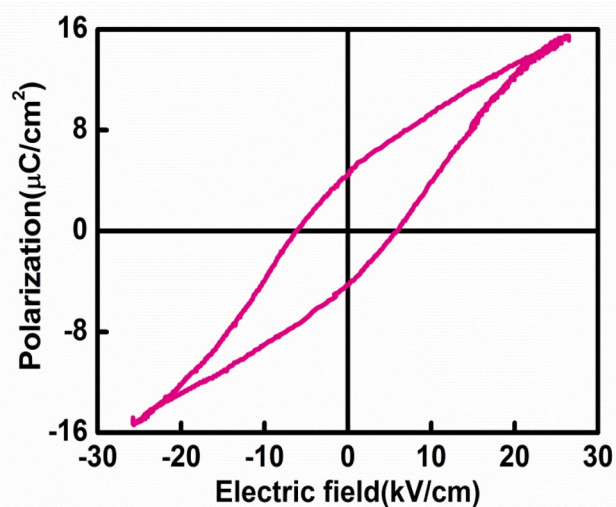


Fig. 9 P-E ferroelectric loop of $\text{Bi}_{0.5}\text{Na}_{0.5}\text{Ti}_{0.80}\text{Sn}_{0.20}\text{O}_3$ compound

of the phase component Q in the circuit element suggest the presence of a modified Debye-type relaxation process. The temperature dependence of AC conductivity suggests the hopping mechanism of charge carriers in the material. The Ohmic current conduction mechanism is found in the compound with reduced leakage current. The analysis of the modulus spectroscopy also supports the non-Debye relaxation mechanism nature in the compound.

References

1. H. Fu, R.E. Cohen, *Nature* **403**, 281 (2000)
2. A.K. Jena, J. Mohanty, *J. Mater. Sci.: Mater. Electron.* **29**, 5150 (2018)
3. C. Kornpom, T. Udeye, T. Bongkarn, *Integr. Ferroelectr.* **177**, 59 (2017)
4. E. Aksel, J.S. Forrester, B. Kowalski, J.L. Jones, P.A. Thomas, *Appl. Phys. Lett.* **99**, 222901 (2011)
5. J. Suchanicz, A. Kania, P. Czaja, A. Budziak, A. Niewiadomski, *J. Eur. Ceram. Soc.* **38**, 567 (2015)
6. N. Kumar, A. Ghosh, R.N.P. Choudhary, *Mater. Chem. Phys.* **130**, 381 (2011)
7. H.L. Yakel, *Acta Cryst.* **8**, 394 (1955)
8. M. Batzill, U. Diebold, *Prog. Surf Sci.* **79**, 47 (2005)
9. J. Robertson, *Rep Prog Phys* **69**, 327 (2006)
10. C. Kilic, A. Zunger, *Phys Rev Lett* **88**, 095501 (2002)
11. K.G. Godinho, A. Walsh, G.W. Watson, *J. Phys. Chem. C* **113**, 439 (2009)
12. V. Purohit, R. Padhee, R.N.P. Choudhary, *Ceram. Int.* **44**, 3993 (2018)
13. R. Das, R. N. P. Choudhary, *J. Mater. Sci., Mater Electron.* **29**, 19099 (2018)
14. A.M.E. Nahrawy, A.M. Mansour, A.B.A. Hammad, A.R. Wassel, *Mater. Res. Express* **6**, 016404 (2019)
15. V. Pal, R.K. Dwivedi, O.P. Thakur, *Curr. Appl. Phys.* **14**, 99 (2014)
16. N. Pradhani, P.K. Mahapatra, R.N.P. Choudhary, *J. Phys.: Mater.* **1**, 015007 (2018)
17. A.A. Azab, A.M. Mansour, G.M. Turkey, *Sci. Rep.* **10**, 4955 (2020)
18. S. Hajra, S. Sahoo, M. De, P.K. Rout, H.S. Tewari, R.N.P. Choudhary, *J. Mater. Sci., Mater Electron.* **29**, 1463 (2018)
19. B. Garbarz-Glos, W. Bąk, M. Antonova, M. Pawlik, *Mater. Sci. Eng.* **49**, 012031 (2013)
20. N. Pradhani, P.K. Mahapatra, R.N.P. Choudhary, *Ceram. Int.* **46**, 4126 (2020)
21. P. Gupta, R. Padhee, P.K. Mahapatra, R.N.P. Choudhary, S. Das, *J. Alloy. Compd.* **731**, 1171 (2018)
22. S. Sahoo, P.K. Mahapatra, R.N.P. Choudhary, M.L. Nandagoswam, *J Mater Sci: Mater Electron* **26**, 6572 (2015)
23. D.K. Mahato, A. Dutta, T.P. Sinha, *Bull. Mater. Sci.* **34**(3), 455 (2011)
24. E.H. El-Khawas, A.A. Azab, A.M. Mansour, *Mater. Chem. Phys.* **241**, 122335 (2020)
25. S. Hajlaoui, I. Chaabane, K. Guidara, *RSC Advances* **94**, 1 (2016)
26. Y.B. Taher, A. Oueslati, M. Gargouri, *J. Alloy. Compd.* **668**, 206 (2016)
27. N. Pradhani, P.K. Mahapatra, R.N.P. Choudhary, R. Giri, *Phys. B* **580**, 411719 (2020)
28. K. Parida, S.K. Dehury, R.N.P. Choudhary, *Phys. Lett. A* **380**, 4083 (2016)
29. T. Paul, A. Ghosh, *Mater. Res. Bull.* **59**, 416 (2014)
30. M.A. Khan, T.P. Comyn, A.J. Bell, *Appl. Phys. Lett.* **92**, 072908 (2008)

Publisher's Note Springer Nature remains neutral with regard to jurisdictional claims in published maps and institutional affiliations.